

Periodic X-ray Sources in the Galactic Bulge: Application of the Gregory-Loredo Algorithm

Tong Bao,^{1,2}[★] Zhiyuan Li,^{1,2}[†]

¹*School of Astronomy and Space Science, Nanjing University, Nanjing 210046, China*

²*Key Laboratory of Modern Astronomy and Astrophysics (Nanjing University), Ministry of Education, Nanjing 210046, China*

Accepted XXX. Received YYY; in original form ZZZ

ABSTRACT

We present the discovery of 23 X-ray periodic sources in the Limiting Window (LW), a low-extinction region in the Galactic bulge, locating 80' south of the Galactic center. Their luminosities range ($10^{31} - 10^{33}$ erg s⁻¹) and period distribution (mostly between 1 to 3 hour), indicate they are cataclysmic variables (CVs). Most of them are determined as magnetic CVs by their feature of period modulation. We also proved that the Gregory-Loredo (GL) method used in this work has better sensitivity and data usage compared to the Lomb-Scargle (LS) method. In combination with the simulation and the geometry of accretion in CVs, we constrain the proportion of polars (IPs) to X-ray sources in LW about 18% (5%) as upper limit.

Key words: Galaxy: bulge — X-rays: stars — X-rays: binaries

1 INTRODUCTION

X-ray-emitting, close binaries, which involve an black hole, a neutron star or a white dwarf (WD) accreting from a companion star, are among the first objects discovered in the X-ray sky and now understood to be ubiquitous in the local universe. As such, X-ray binaries can serve as a useful probe of their parent stellar populations. In particular, cataclysmic variables (CVs), are close binary including a white dwarf (WD) and a main-sequence or sub-giant companion, whose material could be accreted by Roche-lobe overflow or stellar wind. They can be divided into magnetic (mCVs) and nonmagnetic CVs (non-mCVs) according to their magnetic field strengths of WDs. In addition, the mCVs are split into polars ($P_{spin}/P_{orb} \simeq 1$) and IPs ($P_{spin}/P_{orb} \simeq 0.01 - 1$), depending on their level of synchronization. The evolution of CVs are driven by angular momentum losses (AML) to keep the period from expanding, which would made system detached. The existence of "period gap" is caused by the change of mechanism for angular momentum losses. The dominant AML mechanism in long-period systems ($P_{orb} \geq 3$ hour) is "magnetic braking", whereas short-period CVs ($P_{orb} \leq 2$ hour) are driven by gravitational radiation. Meanwhile, there is a minimum period of CVs, resulted from the mass-loss-induced loss of thermal equilibrium in companion star. The orbital period of CVs are mainly between 1 to 10 hours, making it suitable for X-ray timing analysis.

It has been proved that the collective properties of CVs serve as great probe for dynamic interactions of their local environment, contributed from the high abundance of WDs in binaries. The effect would be remarkable only with extremely high stellar density (e.g.

galactic center or global clusters (Cheng et al. 2019)) for us obtaining observable evidence in Hubble time. In addition to that, the individual properties of CVs provide hints for the accretion region and magnetic field, especially from their periodic variability.

It has been suggested that the thousands of X-ray sources in galactic center are magnetic cataclysmic variables, particularly intermediate polars (IPs) (Muno et al. 2009; Zhu et al. 2018). Due to the lack of optical/infrared imaging and spectroscopy resulted from high extinction and source crowding, the direct identification of them has been really difficult. In fact, even the presence and characteristics of the He II $\lambda 4686$ and H β line have been often used to judge if a CV is magnetic or not, the proof is far from conclusive. In Silber (1992), many IPs with weak H β lines could not be identified from non-magnetic systems using this diagnostic. Hence the periodicity becomes a well recognized probe to study their population, because of their different features in periodic modulation (see Section 6.2).

In Muno et al. (2003), eight periodic sources were identified as mCVs in galactic center region (GCR). Then for galactic bulge region, ten periodic sources were found by using Lomb-Scargle methods (Hong et al. 2012). They were believed as an unusual type of mCVs with harder spectra like IPs while their period distribution resembles that of polars. The research was based on the observation of low-extinction Window fields (LW), locating at 1°4 south of the Galactic center. Its rarity of avoiding the obscuration from molecular cloud deserved our deeper excavation of these X-ray sources. Besides, according to RK catalog (Ritter & Kolb 2003), the mCVs (mostly DNe) occupied 20% in CVs sample, while for GCR, this fraction was reckoned over 30-40% (Hailey et al. 2016; Hong et al. 2012). The miss of non-mCVs demands reliable explanation from analyzing the properties of these sources. It may indicates that a

[★] E-mail: baotong@smail.nju.edu.cn

[†] E-mail: lizy@nju.edu.cn

Table 1. *Chandra* observations of the Limiting Window

ObsID	Start Time UT	Nominal R.A. ($^{\circ}$)	Nominal Decl. ($^{\circ}$)	Roll angle ($^{\circ}$)	Exposure ks	Mode
6362	2005-08-19 16:15	267.86875	-29.58800	273	37.7	FAINT
5934	2005-08-22 08:16	267.86875	-29.58800	273	40.5	FAINT
6365	2005-10-25 14:55	267.86875	-29.58800	265	20.7	FAINT
9505	2008-05-07 15:29	267.86375	-29.58475	82	10.7	VFAINT
9855	2008-05-08 05:00	267.86375	-29.58475	82	55.9	VFAINT
9502	2008-07-17 15:45	267.86375	-29.58475	281	164.1	VFAINT
9500	2008-07-20 08:11	267.86375	-29.58475	280	162.6	VFAINT
9501	2008-07-23 08:13	267.86375	-29.58475	279	131.0	VFAINT
9854	2008-07-27 05:53	267.86375	-29.58475	278	22.8	VFAINT
9503	2008-07-28 17:37	267.86375	-29.58475	275	102.3	VFAINT
9892	2008-07-31 08:07	267.86375	-29.58475	275	65.8	VFAINT
9893	2008-08-01 02:44	267.86375	-29.58475	275	42.2	VFAINT
9504	2008-08-02 21:23	267.86375	-29.58475	275	125.4	VFAINT

large number of non-mCVs still awaits discovery since faint class can be always missed in flux-limited surveys.

In this work, we revisit the *Chandra* observations of the LW, employing a novel technique, known as the Gregory-Loredo period searching algorithm, to detect periodic signals in the LW. Meanwhile, the methods with more efficiency and the simulation with higher accuracy have been both operated. We explored the X-ray properties of 23 periodic sources (ten of them identified in [Hong et al. \(2012\)](#)). In Section 2, we describe the preparation of the X-ray data and a raw list of X-ray sources in the LW. We then provide in Section 3 a brief overview of the period searching methods, with an emphasis on the Gregory-Loredo algorithm. main methods for period finding and focuses on the GL method we adopted in this work. Section 4 is devoted to the period searching results. Section 5 presents an X-ray spectral analysis for the detected periodic sources. The comparison with previous work, the identification for these periodic sources and the X-ray source population in the LW would be discussed in Section 6. A summary of this study is given in Section 7.

2 X-RAY DATA PREPARATION

2.1 *Chandra* observations

The LW towards the inner Galactic bulge has been extensively observed by *Chandra* with its Advanced CCD Imaging Spectrometer (ACIS). A total of 13 ACIS-I observations were taken, three in 2005 and ten in 2008, resulting in a total exposure of 982 ks. A log of these observations is given in Table 1. A number of previous studies have made use of all or part of these observations, which primarily focused on the identification of discrete X-ray sources and the quantification of their statistical properties ([Revnivtsev et al. 2009](#); [van den Berg et al. 2009](#); [Hong et al. 2009](#); [Revnivtsev et al. 2011](#); [Hong 2012](#); [Moriwana et al. 2013](#); [Wevers et al. 2016](#)).

We downloaded and uniformly reprocessed the archival data with CIAO v4.10 and CALDB v4.8.1, following the standard procedure¹. The CIAO tool *reproject_aspect* was employed to align the relative astrometry among the individual observations, by matching the centroids of commonly detected point sources. ObsID 9502, which has the longest exposure (164.1 ks), served as the reference

frame. The level 2 event file was created for each ObsID, with the arrival time of each event corrected to the Solar System barycenter (i.e., Temps Dynamique Barycentrique time) by using the CIAO tool *axbary*. We then constructed a merged event list, reprojecting all events to a common tangential point, [R.A., Decl.]=[267.86375, 29.58475]. The individual observations cover a similar field-of-view (FoV) due to their similar aimpoints and roll angles, as illustrated in Figure 1 which displays the merged 2–8 keV counts image. We have examined the light curve of each ObsID and found that the instrumental background was quiescent for the vast majority of time intervals. Hence we preserved all the science exposures for source detection and subsequent timing analysis, taking the advantage of uninterrupted signals within each observation.

2.2 Source detection

It is known that the LW suffers from moderate line-of-sight extinction, $N_H \approx 7 \times 10^{21} \text{ cm}^{-2}$ ([Revnivtsev et al. 2011](#)), which obscures X-ray photons with energies $\lesssim 1 \text{ keV}$. Here we focus on sources prominent in the 2–8 keV band, which are most likely CVs located in the Galactic bulge. This will also facilitate a direct comparison with the CVs found in the Nuclear Star Cluster ([Zhu et al. 2018](#)), the line-of-sight column density of which, $N_H \sim 10^{23} \text{ cm}^{-2}$, is only transparent to photons with energies $\gtrsim 2 \text{ keV}$.

Source detection was performed following the procedures detailed in [Zhu et al. \(2018\)](#). Briefly, we first generated for each observation an exposure map as well as point-spread function (PSF) maps with enclosed count fraction (ECF) of 50% and 90%. Both the exposure and PSF maps were weighted by a fiducial spectrum, which is an absorbed bremsstrahlung with a plasma temperature of 10 keV and a column density of $N_H = 10^{22} \text{ cm}^{-2}$, representative of the X-ray sources in the LW. We then reprojected the individual exposure maps to form a stacked exposure map in the same way as for the counts images; the PSF maps were similarly stacked, weighted by the corresponding exposure map. Next, we employed *wavdetect* to identify discrete sources in the merged 2–8 keV counts image, supplying the algorithm with the stacked exposure map and the 50%-ECF PSF map and adopting a false-positive probability threshold of 10^{-6} . This resulted in a raw list of 847 independent sources in the 2–8 keV band.

The source centroid derived from *wavdetect* was refined using a maximum likelihood method that iterates over the detected counts within the 90% enclosed counts radius (ECR). Starting from this

¹ <http://cxc.harvard.edu/ciao>

step we consider the 1–8 keV band to maximize the signal from potential sources in the LW. Then, for each ObsID, source counts were extracted from the 90% ECR, while background counts were extracted from a concentric annulus with inner-to-outer radii of 2–4 times the 90% ECR, excluding any pixel falling within 2 times the 90% ECR of neighboring sources. Source crowding is not a general concern for the LW, but in a few cases the source extraction region was reduced to 50% ECR due to otherwise overlapping sources. The total source and background counts were obtained by summing up the individual observations. Photometry (i.e., net photon flux and its error) for individual sources were calculated using the CIAO tool *aprates*, which takes into account the local effective exposure, background and ECF. We consider a *significant detection* for a given source in a given ObsID if the photon flux is greater than 3 times the error. We further define for each source an inter-observation *variability index*, $VI = S_{\max}/S_{\min}$, where S_{\max} and S_{\min} are the maximum and minimum photon fluxes among all the significant detections, respectively. This implicitly requires significant detections in at least two observations.

3 PERIOD SEARCHING METHOD

In this section, we first provide our motivation of employing the Gregory-Loredo (GL) algorithm, followed by an outline of its basic principles (Section 3.1). We then describe our application of the GL algorithm to the *Chandra* data of the LW (Section 3.2). This is complemented by a set of simulations to evaluate the detection (in)completeness of periodic signals (Section 3.3).

3.1 The Gregory-Loredo Algorithm

There exists in the literature a variety of period searching methods, which can be broadly divided into three categories according to their working principles.

The most traditional method is based on Fourier transform and its power density spectra, which includes the classical Schuster periodogram (Schuster 1898), the Fourier analysis with unequally-spaced data (Deeming 1975), the correlation-based method (Edelson & Krolik 1988), among others.

Another widely-used method seeks to fit the data with a periodic model in the frequency space, employing statistics such as least-squares residuals to define the likelihood function and then selecting the frequency that maximizes the likelihood. The famous Lomb-Scargle periodogram (Lomb 1976; Scargle 1982, hereafter LS) belongs to this category. Note that when adopting trigonometric functions, the least-squares method falls into the Fourier transformation category. Another variant is to replace the least-squares residuals with polynomial fits, such as that used in Schwarzenberg-Czerny (1996).

The last category is the phase-folding method. For each trial period the time-tagged data is folded as a function of phase, and the best-fit period is found by optimizing the cost function through the frequency space. The cost function is designed to evaluate how much the phase-folded light curve deviates from constant. Methods belonging to this category use diverse cost functions. Several widely known examples are the Epoch Folding (EF) algorithm (Leahy et al. 1983), the Phase Dispersion Minimization (Stellingwerf 1978), and the GL algorithm (Gregory & Loredo 1992).

In X-ray studies, the detection of periodic signals is often involved with irregularly and sparsely sampled data. When working in frequency space, such a sampling can lead to spurious signals

and heavy contamination to the real signal. Phase-folding methods, on the other hand, can minimize the effect of irregular data since the cost function excludes the dead time and can compensate for observation gaps. Moreover, the number of detected source counts is often only moderate. While one can in principle apply binning to create photometric light curves, it takes the price of potentially losing temporal information. Phase-folding methods, on the other hand, directly handle individual events, thus maximally incorporating the temporal information.

Most X-ray sources in the LW share the characteristics of irregular sampling and limited source counts. Therefore, it is appropriate to employ the GL algorithm, which applies the Bayesian probability theory to the phase-folded light curve, to search for periodic signals for the LW sources. We provide a brief summary in mathematical form of Bayes’s theorem and the GL algorithm in Appendix A. The key of this algorithm is the multiplicity of the phase distribution of events,

$$W_m(\omega, \phi) = \frac{N!}{n_1! n_2! n_3! \cdots n_m!}. \quad (1)$$

Here N represents the total number of counts of a given source, $n_i(\omega, \phi)$ is the number of events falling into the i th of m phase bins, given the frequency ω and phase ϕ , satisfying $\sum_{i=1}^m n_i(\omega, \phi) = N$.

The multiplicity is the number of ways that the binned distribution could have arisen by chance. It can be easily shown that the more the values of n_i differ from each other, the smaller the multiplicity. In other words, the more the stepwise model defined the m phase bins deviates from constant, the more likely there exists a periodic signal, the probability of which is inversely proportional to the multiplicity.

In general, the GL algorithm takes the following steps:

- (i) Compute the multiplicity for all sets of (m, ω, ϕ) (Eqn. 1). In this work, the highest value of m is set to be 12.
- (ii) Given m , integrate over the (ω, ϕ) space and calculate the so-called “odds ratio” using Bayes’s theorem (Eqn. A16). The “odds ratio” determines the ratio of probabilities between a periodic model and a non-periodic (constant) model. The range of ω depends on the source of interest and is further addressed in Section 3.2.
- (iii) Sum up the normalized odds ratios of each m to determine the probability of a periodic signal (Eqn. A20). If this probability exceeds a predefined threshold (default at 90%), a periodic signal is favored.
- (iv) Finally, compare all the odds ratios integrated over the ϕ space, finding the value of ω with the highest odds ratio, which then gives the period $P = 2\pi/\omega$ (Eqn. A21).

3.2 Application to the LW

We apply the GL algorithm to search for periodic signals in the LW sources. For a given source, the 1–8 keV counts within the 90% ECR of individual ACIS-I observations are extracted to form a time series. In addition, we supply for each source the information of “epoch”, i.e., the start time and end time of each ObsID in which the source has at least one detected count. This information is used to compensate for the uneven distribution over the phase bins (see Eqn. A17 for a detailed illustration). Since the GL algorithm determines the probability of a periodic signal against a constant light curve, there is no need to separately account for the background level, which is absorbed into the constant. Nevertheless, we have measured the local background (Section 2.2) for each periodic source as a consistency check (see Section 4).

As mentioned in Section 3.1, the GL algorithm folds the time



Figure 1. 2–8 keV counts image of the Limiting Window, combining 13 *Chandra*/ACIS-I observations. Locations of the 23 periodic sources are marked with colored circles (*magenta*: ten sources previously reported by [Hong et al. 2012](#); *red*: thirteen newly discovered in this work). Source numbering is the same as in Table 2. In particular, 1/14 and 21/22 are the two sources each showing two periodic signals.

series at a trial frequency (or period). In practice, the resolution and range of frequency must be compromised between efficiency and computational power. Thus we restrict our analysis on three period ranges: (300, 3000), (3000, 10000) and (10000, 50000) sec, with a frequency resolution of 10^{-7} , 10^{-8} and 10^{-9} Hz, respectively. The period ranges are chosen based on the expectation that most, if not all, detectable periodic X-ray sources in the LW should be CVs. The orbital period distribution of CVs is known to exhibit a minimum at ~ 82 minutes, a gap between 2–3 hours, and a maximum around 10 hours ([Knigge et al. 2011](#)). The second and third period ranges well cover these characteristic periods, whereas the first range probes the spin period of fast rotating IPs. Given the timespan of $\sim 10^8$ sec between the first and last ACIS-I observations, the chosen frequency resolutions are optimal for an efficient search of periodic signals.

3.3 Detection completeness

For a given period searching algorithm, the detection rate depends on both the number of observed counts, the intrinsic shape of the light curve, as well as the observing cadence. To quantify the detection rate and hence gain insight on the nature of the periodic sources in the LW, we perform simulations following the merit of [Cicuttin et al. \(1998\)](#). Two functional forms of light curve are considered: a sinusoidal function and a piecewise function. While these are admittedly idealized shapes, they can represent realistic light curves, e.g., the former resulted from rotational modulation and the latter due to eclipse.

A sinusoidal light curve follows,

$$\lambda(t) = \lambda_0 [1 + A_0 \sin(\omega t + \phi)], \quad (2)$$

where $\omega = 2\pi/P$, A_0 is the relative amplitude of variation, and

λ_0 is the mean count rate which may include contribution from a constant background. The phase ϕ can be arbitrarily set at zero. For a direct comparison with observations, we relate λ_0 to the total number of counts, $C = \lambda_0 T_{\text{exp}}$, where T_{exp} is the exposure time. This holds since T_{exp} is typically much longer than the modulation period (P). The simulations are run with a selected number of parameters due to constraints in computational power. Specifically, we adopt $C=50, 100, 200, 300, 400$ and 500 , $A_0=0.5, 0.6, 0.7, 0.8$ and 0.9 , and $P=554, 5540$ and 45540 sec, resulting in a total of $6 \times 5 \times 3 = 90$ combinations. The chosen periods are representative of the actually searched ranges (Section 3.2), whereas the adopted total counts well sample the range of observed counts in the LW sources.

We thus simulate 100 light curves for each combination of parameters, taking into account Poisson errors and the exact start and end times of the 13 ACIS-I observations. The arrival time of each simulated count is further randomly modified by an amount of 3.2 sec to mimic the effect of ACIS frame time. The simulated light curve is then searched for a periodic signal using the GL algorithm in the same manner as for the real data (Section 3.2). We count a valid detection if the found period has a detection probability greater than 90% and its value is consistent with the input period to within 1%. We notice that in a small fraction of simulated light curves of the shortest input period (554 sec), the second harmonics (i.e., 2 times the true period) is detected with an even higher probability than the true period. We also consider such cases a valid detection as long as the true period itself fulfills the above criteria.

The detection rate for a given combination of parameters is taken to be the fraction of the 100 simulated light curves having a valid detection. The top, middle and bottom panels of Figure 2 show the result of the three test periods, respectively, in which several trends are apparent. First and intuitively, for a given period and amplitude, higher total counts would lead to higher detection rates, while for given total counts, a higher amplitude also leads to a higher detection rate. The simulation results confirm these expectations. Second, for the same total counts and amplitude, the detection rate is generally higher for a longer period. This can be understood as due to a statistical behavior in the multiplicity (Eqn. 1), which has a lower value for a longer period. This holds for both the sinusoidal and piecewise light curves. Lastly, for total counts of 50, the detection rate is almost always below 10% regardless of the period and amplitude.

The piecewise function, which mimics an eclipse against an otherwise constant flux, takes the form of

$$\lambda(t) = \begin{cases} \lambda_0 & \phi(t) \in [0, (1-w)\pi) \cup ((1+w)\pi, 2\pi], \\ f\lambda_0 & \phi(t) \in [(1-w)\pi, (1+w)\pi], \end{cases} \quad (3)$$

where w accounts for the eclipse width (duration) in phase space, and f characterizes the relative depth of the eclipse ($0 \leq f \leq 1$; $f = 0$ corresponds to total eclipse). Here the middle of eclipse is assumed to occur at $\phi = \pi$. Again, λ_0 can be related to the total counts as $C = [1 - (1-f)w]\lambda_0 T_{\text{exp}}$. We set $f = 0.1$ and $w = 0.1$ in our simulations, which are not atypical of eclipsing CVs. We test three values of the period, $P=5258, 15258$ and 45258 sec and adopt trial count rates $\lambda_0 = 1, 2, 3, 4, 5, 6, 7, 8, 9, 10, 15$ and 20×10^{-4} cts s^{-1} . For each combination of parameters, 100 simulated light curves are again generated and fed to the GL algorithm. The resultant detection rate is shown in Figure 3. As expected, the detection rate is generally higher for a longer period. It can also be seen that for total counts below ~ 300 , the detection rate is $\lesssim 10\%$ regardless of the period; only when total counts exceed ~ 1500 , the detection rate becomes 100% for all test periods. Since only a small number of sources in

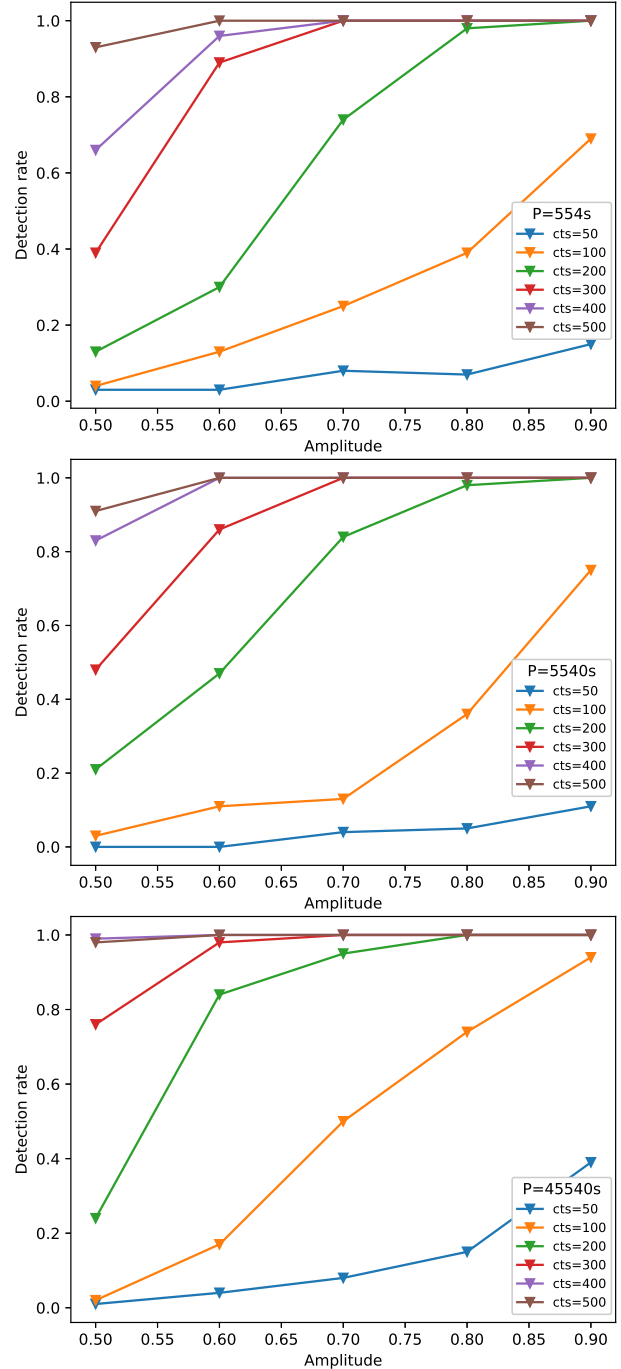


Figure 2. Detection rates as a function of relative variation amplitude, based on simulated sinusoidal light curves. The top, middle and bottom panels are for modulation period of 554, 5540 and 45540 sec, respectively. The different colored symbols and lines represent different values of total counts, as labeled.

the raw list have total counts more than 1500, we expect a relatively low detection rate of eclipsing sources in the LW.

We have also run simulations to estimate the rate of false detection, which refers to the detection of a periodic signal from an intrinsically non-periodic (e.g., constant) light curve. Considering that most LW sources can have a low-amplitude long-term variation, we approximate a non-periodic light curve with a sinusoidal function with $P=5$ yr and $A_0=0.5$. Simulated light curves are generated



Figure 3. Detection rates as a function of total counts, based on simulated piecewise light curves. Different colored symbols and lines represent different periods, as labeled.

with totals counts from 50 to 5000 and fed to the GL algorithm. No false detection of periodic signals, at any value between 300–50000 sec, is found. Therefore, it seems safe to conclude that the false detection rate is essentially zero for the GL algorithm applied to the LW data.

4 PERIOD SEARCHING RESULTS

According to the simulations in Section 3.3, a periodic signal is hard to detect in LW sources with total counts $C < 100$, even in the case of high variation amplitudes. Therefore, we restrict our period searching to sources with 1–8 keV total counts $C \geq 100$, which include 667 of the 847 sources in the raw list. Among these 667 sources, 25% (4%) have $C \geq 500$ (1000).

Adopting a probability threshold of 90%, we initially obtain 48 tentative periodic signals from the three searched period ranges. However, it is necessary to filter spurious detections, which may be caused by several effects:

(i) By design, the ACIS is dithered to distribute photons over more CCD pixels to avoid pile-up and to fill CCD gaps. The dither period is 706.96 s in pitch and 999.96 s in yaw. Any signal detected at these two periods and their harmonics are thus excluded. These are mostly found in sources located close to CCD gaps, where dithering significantly reduces the number of detected counts in a periodic fashion.

A related concern is how dithering would affect the detection of genuine periods. We run simulations to test this effect. Specifically, we generate simulated sinusoidal light curves with $P = 5072.97$ sec and $C = 293$. This choice is motivated by one particular periodic source (#5 in Table 2), which has a fractional detector coverage of 0.74 (in other words, 26% of the intrinsic flux is lost due to dithering into the CCD gap), the lowest among all valid periodic sources. The dithering effect is mimicked by artificially removing the simulated counts according to a probability distribution calculated by the CIAO tool *dither_region*. No difference is found in the resultant detection rate, compared to that without dithering.

(ii) In certain sources, multiple detections can be caused by second and third harmonics of the same intrinsic signal (i.e., 2 and 3 times the true period). These can be easily identified by the sign of

double-peak or triple-peak in the phase-folded light curve, provided that the intrinsic signal has a single-peaked structure.

However, the intrinsic structure might be double-peaked, in which case it is more difficult to distinguish between the true period and the half harmonic (i.e., half the true period), in particular when the two peaks have a similar strength and width. Generally speaking, the double-peaked shape only occurs in IPs producing hard X-rays near both magnetic poles (see Section 6.2 for more discussions). When viewed from certain angle, the two poles alternatively drift across the front side of the WD, producing the double-peaked X-ray light curve. The modulation period in this case must be the spin period of the WD, typically under one hour. Among our tentative detections, most of those showing a double-peaked light curve have a corresponding period longer than 3 hours, far beyond the empirical range of spin periods of IPs. These are probably second harmonics rather than a genuine spin period. Hence we assume that there is no half harmonics in the LW sources and always take the lowest period as the true period. This assumption is supported by our extensive simulations presented in Section 3.3, in which no half harmonic (the true period is known before hand) is found.

(iii) Strong flux variations or outbursts occupying one particular observation can also cause a fake periodic signature. This is because the GL algorithm, which analyzes the phase-folded light curve, can be fooled if there were too many photons found in a single observation, producing excess in certain phase bins. In this case the algorithm may “think” there exists a period especially in the range of (10000, 50000) sec. Among the sources with tentative periods, four exhibit a variability index $VI > 10$, indicating strong variations. We thus reanalyze their light curves using two subsets of observations: those covering only the outburst and those excluding the outburst. For three of them, the tentative period cannot be recovered in either subset. Therefore, these three are probably fake signals. The remaining source is retained since its period can be recovered in both the outbursting and quiescent subsets.

The above filtering thus results in 25 valid periodic signals in 23 sources. Among them, 10 signals were previously reported by Hong et al. (2012) and are confirmed here with the GL algorithm, while the remaining 15 periods are new discoveries (a comparison between our work and Hong et al. 2012 is further addressed in Section 6.1). The basic information of these periodic sources are listed in Table 2, sorted by the order of increasing period. The source locations are marked in Figure 1.

There are two sources each exhibiting dual periods, hence we have assigned each of them two IDs: #1/#14 and #21/#22. The phase-folded light curves at the two modulation periods are shown for source #1/#14 in the upper panels of Figure 4 and for source #21/#22 in the upper panels of Figure 5. The number of phase bins, between 20 to 50, is chosen to optimally display substructures in the light curve. While the GL algorithm does not rely on quantifying the local background, for comparison we plot in these panels the estimated background level (yellow strip, the width of which represents 1σ Poisson error). We defer discussions on the light curve shape, which contains important information on the nature of the periodic source, to Section 6.2.

The phase-folded light curves are complemented by the long-term, inter-observation light curve, shown in the lower left panel of Figures 4 and 5, and by the source spectrum (see Section 5), shown in the lower right panel of Figures 4 and 5. Similar figures of the remaining 21 sources are presented in Appendix B.

Table 2. Basic information of the periodic X-ray sources in the Limiting Window

ID LW (1)	R.A. ° (2)	Decl. ° (3)	Period s (4)	Prob. (5)	C (6)	C _B (7)	VI % (8)	H-ID (9)	Harmonics (10)	Class (11)
1 [†]	267.77173	-29.61332	853.83	0.90277	202	95.5	1.92	-	-	IP
2	267.76657	-29.57529	3820.83	0.99222	902	116.4	1.94	-	-	IP?
3	267.82829	-29.63660	4728.90	1.00000	394	58.3	2.13	H6	Third	IP?
4	267.94766	-29.70427	4886.79	0.99994	784	413.2	1.90	H8	-	polar?
5	267.86255	-29.61859	5072.97	0.99933	293	12.9	2.34	-	Second	polar?
6	267.84831	-29.63212	5130.57	1.00000	437	47.2	2.51	H2	Second	polar?
7	267.86651	-29.58575	5144.97	0.99880	335	19.8	2.48	-	Second	IP?
8	267.90982	-29.55845	5158.75	1.00000	121	30.6	2.30	-	Second	polar?
9	267.88075	-29.48562	5231.49	0.94949	347	188.4	1.65	-	-	polar?
10	267.91616	-29.66900	5252.93	0.91425	211	134.8	-	-	-	polar?
11	267.83116	-29.61651	5261.93	1.00000	438	28.0	1.46	H10	Second	IP?
12	267.73141	-29.49721	5334.76	0.99952	760	603.4	1.25	-	Second	polar?
13	267.96901	-29.58142	5501.16	0.99094	512	124.9	2.89	-	-	polar?
14 [†]	267.77173	-29.61332	5608.21	0.96821	202	95.5	1.92	-	Third	IP
15	267.89161	-29.46508	6335.85	1.00000	823	322.6	2.09	H5	Second	polar?
16	267.89024	-29.55369	6597.55	1.00000	487	24.3	4.30	H9	Second	polar?
17	267.87162	-29.49011	7448.98	0.99999	535	157.3	1.76	H3	Second	polar?
18	267.78806	-29.58177	7756.19	0.99941	214	54.5	4.76	-	Second	IP?
19	267.88203	-29.49922	8546.28	1.00000	3402	132.7	3.27	H4	Second	IP?
20	267.82785	-29.50770	8844.82	0.90987	263	89.9	1.82	-	Second	IP?
21 [‡]	267.96375	-29.55290	9877.52	0.99992	1963	153.1	1.44	-	-	IP
22 [‡]	267.96375	-29.55290	10342.30	1.00000	1963	153.1	1.44	H1	-	IP
23	267.84487	-29.57680	12002.70	1.00000	307	13.8	1.86	H7	Second	polar?
24	267.90974	-29.71112	42219.03	1.00000	1039	343.0	23.6	-	-	IP?
25	267.83142	-29.65992	47317.12	0.98850	138	77.0	-	-	-	AB

Notes: (1) Source sequence number assigned in the order of increasing period. The same source with dual periods is marked by [†] and [‡]. (2) and (3) Right Ascension and Declination (J2000) of the source centroid. (4) The modulation period determined by the GL algorithm. (5) The probability of the periodic signal defined by Eqn. A20. (6) The number of total counts in the 1–8 keV band. (7) The number of estimated background counts. (8) The long-term variability index, defined as $VI = S_{\max}/S_{\min}$, where S_{\max} and S_{\min} are the maximum and minimum photon fluxes among all the valid detections. Sources #10 and #25 have no measurable VI. (9) The ID of previously detected periodic signals as given in table 2 of Hong et al. (2012). (10) Significant harmonics, if existed. (11) Source classification based primarily on the phase-folded light curve.

5 X-RAY SPECTRAL ANALYSIS

We perform spectral analysis for all 23 confirmed periodic sources to gain insight on their nature. Source and background spectra are extracted from the same regions as described in Section 2.2, along with the ancillary response files (ARFs) and redistribution matrix files (RMFs), by using the CIAO tool *specextract*. The spectra from individual observations are then coadded to form a combined spectrum of a given source, with the corresponding ARFs and RMFs weighted by the effective exposure. Further, the spectrum is adaptively binned to achieve a minimum of 20 counts and a signal-to-noise ratio (S/N) greater than 2 per bin. The resultant spectra are analyzed using XSPEC v12.9.1.

Since these sources are expected to be CVs, we adopt a fiducial spectral model, which consists of a bremsstrahlung continuum and three Fe lines (Zhu et al. 2018; Xu et al. 2019). We model each line with a Gaussian profile, fixing their line centroid at 6.40, 6.68 and 6.97 keV, respectively, and adopting a zero line width. All model components are subject to an unknown line-of-sight absorption (*phabs* in XSPEC).

It turns out that the plasma temperature (T_b) is not well constrained in most sources, due to a moderate spectral S/N and the insufficient sensitivity of *Chandra* at energies above 8 keV. Hence for such cases we fix T_b at 40 keV, which is typical of IPs when their hard X-ray (up to tens of keV) spectra are available (Xu et al. 2016;

Hailey et al. 2016). Setting a lower value of T_b , for instance, at 20 keV, does not affect our following conclusions.

Physically, the three lines (hereafter referred to as the 6.4, 6.7 and 7.0 keV lines) correspond to neutral Fe $K\alpha$, Fe XXV $K\alpha$ and Fe XXVI $Ly\alpha$, respectively, which are among the most commonly detected emission lines in CV spectra. The latter two lines, in particular, arise from the post-shock plasma near the WD surface, and their flux ratio ($I_{7.0}/I_{6.7}$) has proven to be a robust tracer of the plasma temperature, hence also a good indicator of the WD mass (Xu et al. 2016). Unfortunately, again due to the limited number of counts, the Fe lines insignificant in most of the 23 sources. Only one sources, #21 (same as #22), shows a significant ($\geq 3\sigma$) line at all three energies. The 7.0 and 6.7 keV lines have a flux ratio of $I_{7.0}/I_{6.7} = 0.91^{+1.22}_{-0.56}$ (90% errors), but the uncertainty is too large for a meaningful constraint on the WD mass. Three additional sources (#2, #20 and #23) show a significant 6.7 keV only.

Results of the spectral analysis are summarized in Table 3. We have also derived the 1–8 keV unabsorbed luminosity based on the best-fit model and assuming a uniform distance of 8 kpc. It is noteworthy that source #24 has an absorption column density of $0.4^{+0.2}_{-0.1} \times 10^{21} \text{ cm}^{-2}$, significantly lower than the expected column density of the LW, $N_H \geq 7 \times 10^{21} \text{ cm}^{-2}$ (Revnivtsev et al. 2011). Hence this source may be located in the foreground, and its true luminosity can be substantially lower than that listed in Table 3.

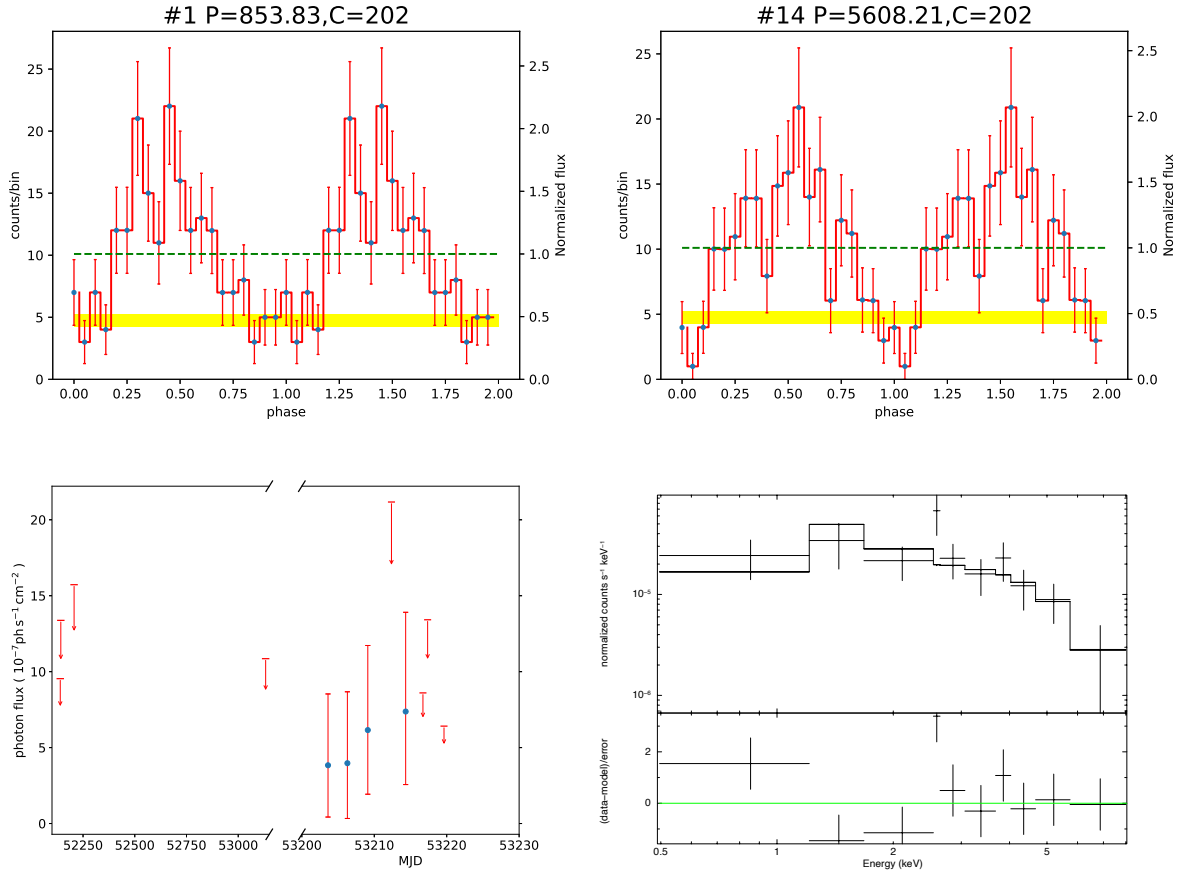


Figure 4. *Upper panels:* The 1–8 keV phase-folded light curves of source #1/#14 at the two modulation periods. The green dashed line represents the mean count rate, whereas the yellow strip represents the local background, the width of which represents 1σ Poisson error. *Lower left:* the 1–8 keV long-term, inter-observation light curve. Arrows represent 3σ upper limits. *Lower right:* Source spectrum and the best-fit model. See text for details.

6 DISCUSSION

In this section, we discuss the most significant implications of our results. We first provide a comparison between our work and [Hong et al. \(2012\)](#) (Section 6.1). Then, we try to classify the periodic sources based on their temporal and spectral properties, demonstrating that the majority of these sources are most likely magnetic CVs (Section 6.2). Lastly, we attempt to constrain the fraction of various CV sub-classes in the Galactic bulge (Section 6.3).

6.1 Comparison with previous work

We have detected 25 periodic signals from 23 sources in the LW (Table 2). Our detections fully recover the 10 periodic signals from 10 sources found by [Hong et al. \(2012\)](#). As illustrated in the upper panel of Figure 6, the measured periods of these 10 signals from the two studies agree with each other to within 0.7% and show no systematic bias. The remaining 15 periods are new detections. Since our work and [Hong et al. \(2012\)](#) have used the same set of *Chandra* observations, this difference must be owing to the different period searching methods employed.

[Hong et al. \(2012\)](#) employed the LS periodogram, which, as described in Section 3.1, handles the photometric light curve, while the GL algorithm processes the phase-folded light curve with tolerance for observation gaps. We have applied the LS periodogram

to our data in essentially the same way as [Hong et al. \(2012\)](#) and confirmed that only those 10 periods found in their work can be detected by this method. The other 15 periods do not result in a significant detection in the LS periodogram, mainly due to its low efficiency with low-count sources. The detection rate never exceeds 20% for net counts $\lesssim 150$, according to the simulations presented in [Hong et al. \(2012, figure 7 therein\)](#).

For comparison, we provide an estimate on the detection rate of the 10 commonly detected periodic signals using the GL algorithm. For practical purposes we assume an intrinsic sinusoidal shape (Eqn. 2), for which the total counts and period are taken directly from the observed values, whereas the relative amplitude (A_0) is taken from [Hong et al. \(2012\)](#), which was based on the Rayleigh statistics ([Buccheri et al. 1983; Munro et al. 2003](#)). For each of the 10 signals, 100 simulated light curves are produced and fed to the GL algorithm. Again, we take the 90% probability threshold and a period accuracy of 1% to define a valid detection. The percentage of valid detections, P_{det} (also listed in column 9 of Table 2), is plotted in the upper panel of Figure 6, along with the detection rate of the LS periodogram taken from [Hong et al. \(2012\)](#). Clearly, the GL algorithm works better in almost all cases compared to the LS periodogram.

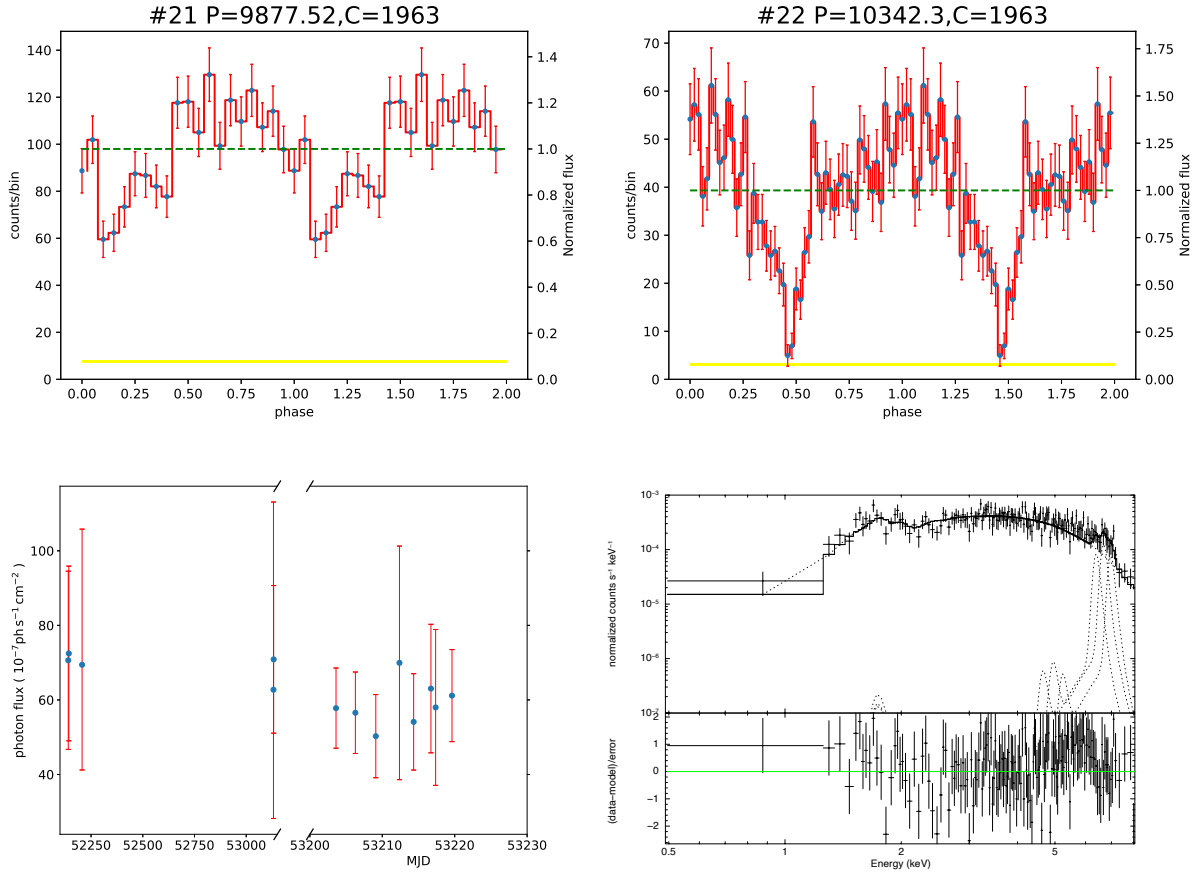


Figure 5. Similar to Figure 4, but for source #21/#22.

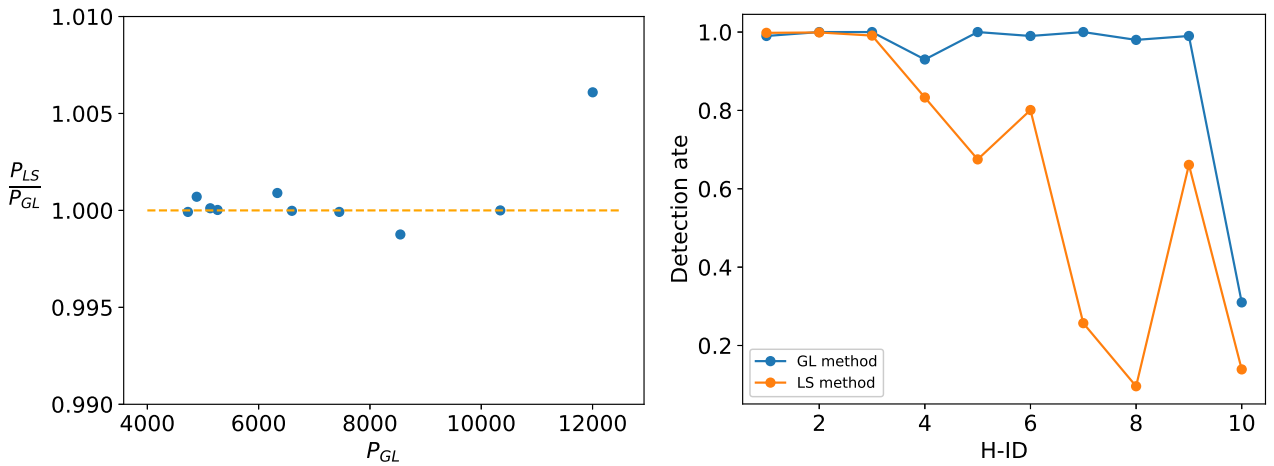


Figure 6. Comparison between the period (left) and detection rate (right) of the 10 signals commonly found by the GL algorithm (this work) and the LS periodogram (Hong et al. 2012). The H-ID is the sequence number given in Hong et al. (2012), same as listed in column 6 of Table 2.

6.2 Classifying the periodic X-ray sources

While it is generally difficult to unambiguously identify the nature of an X-ray source without knowing its optical counterpart, which is the case for most LW sources, the X-ray temporal and spectral properties of the 23 periodic sources contain useful information that actually allow for a reasonable classification for many of them.

First of all, all but one (#25) of these sources are found in the 1–8 keV luminosity range of $10^{31} - 10^{33} \text{ erg s}^{-1}$ (Table 3), which is typical of CVs. On the contrary, coronally active binaries (ABs), which are thought to dominate the detected X-ray sources in the LW by number (Revnivtsev et al. 2009), generally have unabsorbed X-ray luminosities below $10^{31} \text{ erg s}^{-1}$ (Sazonov et al.

Table 3. X-ray spectral properties of the periodic sources

ID	N_{H}	T_{b}	$EW_{6.7}$	$I_{6.7}$	$\chi^2/\text{d.o.f}$	L_{1-8}
(1)	(2)	(3)	(4)	(5)	(6)	(7)
LW	10^{22} cm^{-2}	keV	keV	$10^{-7} \text{ ph cm}^{-2} \text{ s}^{-1}$		$10^{31} \text{ erg s}^{-1}$
1 [†]	$0.5^{+0.8}_{-0.3}$	40 (fixed)	-	-	0.72/8	$2.0^{+0.7}_{-0.6}$
2	$2.2^{+0.5}_{-0.5}$	21^{+57}_{-10}	$0.6^{+1.2}_{-0.3}$	2^{+1}_{-1}	0.86/78	26^{+3}_{-2}
3	$1.4^{+0.4}_{-0.3}$	40 (fixed)	-	-	0.98/35	7^{+1}_{-1}
4	$1.2^{+0.7}_{-0.5}$	11^{+53}_{-5}	-	-	0.91/27	25^{+3}_{-5}
5	$1.0^{+0.3}_{-0.2}$	40 (fixed)	-	-	1.00/35	$6.2^{+0.9}_{-0.8}$
6	$1.8^{+0.6}_{-0.5}$	7^{+12}_{-3}	-	-	1.12/42	10^{+1}_{-1}
7	$1.6^{+0.6}_{-0.5}$	42^{+43}_{-32}	-	-	0.86/39	7^{+1}_{-1}
8	2^{+2}_{-1}	40 (fixed)	-	-	0.93/7	$2.0^{+0.6}_{-0.5}$
9	1^{+1}_{-1}	21^{+96}_{-20}	-	-	1.10/7	4^{+1}_{-1}
10	3^{+7}_{-2}	40 (fixed)	-	-	0.85/5	2^{+2}_{-1}
11	$1.9^{+0.4}_{-0.3}$	40 (fixed)	-	-	1.22/47	11^{+1}_{-1}
12	6^{+10}_{-4}	40 (fixed)	-	-	0.78/6	8^{+6}_{-3}
13	$0.9^{+0.3}_{-0.2}$	40 (fixed)	-	-	1.15/38	9^{+1}_{-1}
14 [†]	$0.5^{+0.8}_{-0.3}$	40 (fixed)	-	-	1.14/5	$2.0^{+0.7}_{-0.6}$
15	$1.5^{+0.5}_{-0.4}$	40 (fixed)	-	-	1.16/42	14^{+2}_{-2}
16	$0.9^{+0.2}_{-0.2}$	40 (fixed)	-	-	1.43/51	$9.4^{+0.9}_{-0.9}$
17	$2.7^{+0.6}_{-0.5}$	40 (fixed)	-	-	0.75/36	13^{+2}_{-2}
18	$2.0^{+0.9}_{-0.7}$	40 (fixed)	-	-	0.53/14	5^{+1}_{-1}
19	$1.8^{+0.1}_{-0.1}$	40 (fixed)	-	-	0.95/185	93^{+4}_{-4}
20	2^{+2}_{-1}	4^{+28}_{-3}	-	$1.4^{+0.9}_{-0.8}$	1.04/12	6^{+2}_{-2}
21 [‡]	$2.8^{+0.3}_{-0.2}$	40 (fixed)	$0.6^{+0.2}_{-0.2}$	3^{+2}_{-1}	1.10/147	67^{+4}_{-3}
22 [‡]	$2.8^{+0.3}_{-0.2}$	40 (fixed)	$0.6^{+0.2}_{-0.2}$	3^{+2}_{-1}	1.10/147	67^{+4}_{-3}
23	$1.8^{+0.4}_{-0.4}$	40 (fixed)	$1.2^{+0.7}_{-0.6}$	$1.3^{+0.8}_{-0.6}$	1.43/37	10^{+1}_{-1}
24	$0.4^{+0.2}_{-0.1}$	5^{+4}_{-2}	-	-	1.19/55	10^{+1}_{-1}
25	1^{+3}_{-1}	2^{+2}_{-1}	-	-	0.80/2	$0.8^{+0.3}_{-0.3}$

Notes: (1) Source sequence number as in Table 2. †#1 and #14 are the same source with two different periods; ‡#21 and #22 are the same source with two different periods. (2) Line-of-sight absorption column density. (3) The bremsstrahlung temperature, in units of keV. Fixed at a value of 40 keV if the spectrum provides no significant constraint to this parameter. (4) Equivalent width of the 6.7 keV line. (5) Integrated flux of the 6.7 keV line. (6) χ^2 and degree of freedom of the best-fit model. (7) 1–8 keV unabsorbed luminosity, corrected for the enclosed-energy fraction. Quoted errors are at the 90% confidence level.

2006). This stems from the empirical fact that the coronal X-ray emission from low-mass stars saturates at $\sim 10^{-3}$ of the bolometric luminosity (Güdel 2004). The X-ray spectra of these sources are less informative, since except in a few cases they lack the unambiguous sign of Fe lines due to the moderate S/N (Section 5), which otherwise would be another characteristic signature of CVs (e.g., Xu et al. 2016). Nevertheless, most of these sources do show a very hard continuum that are again typical of CVs. Furthermore, the vast majority of the detected periods fall between 1.1–3.3 hours, consistent with the range of short-period CVs in the solar neighborhood (Ritter & Kolb 2003), i.e., those having an orbital period between the so-called period minimum and the upper bound of the period gap, as illustrated in Figure 7. Therefore, the global X-ray properties point to CVs dominating the detected periodic sources, a conclusion also drawn by Hong et al. (2012).

It will then be interesting to ask to which sub-class of CVs these periodic sources belong. The phase-folded light curves may provide useful hints to this question. In magnetic CVs, including polars and IPs, their spin modulations can give rise to a characteristic light

curve. For polars, let us consider the simplistic situation in which hard X-rays (photon energy $\gtrsim 1$ keV) are produced in only one of the two magnetic poles². Denoting i the angle between the line-of-sight and the spin axis, β the angle between the spin and magnetic axes, and ϵ the magnetic colatitude of the accretion column, when $i + \beta + \epsilon > 90^\circ$, the two poles will alternately drift across the front side of the WD. The resultant light curve will look like that of source #6, #8 and #10, with nearly half of the cycle showing a valley of near-zero hard X-ray flux (Heise et al. 1985). The periods of these sources are consistent with the period range of known polars (for polars the orbital and spin periods are equal; Figure 7). This so-called “two-pole” behavior becomes more complicated if some hard X-rays were also produced near the second pole, in which case the “valley” is partially filled, resulting in a light curve like that of

² In this picture, accretion can still take place in the other pole, in fact, at a much higher accretion rate, producing quasi-black-body emission peaking at the soft X-ray and extreme ultraviolet bands (Hellier 2001).

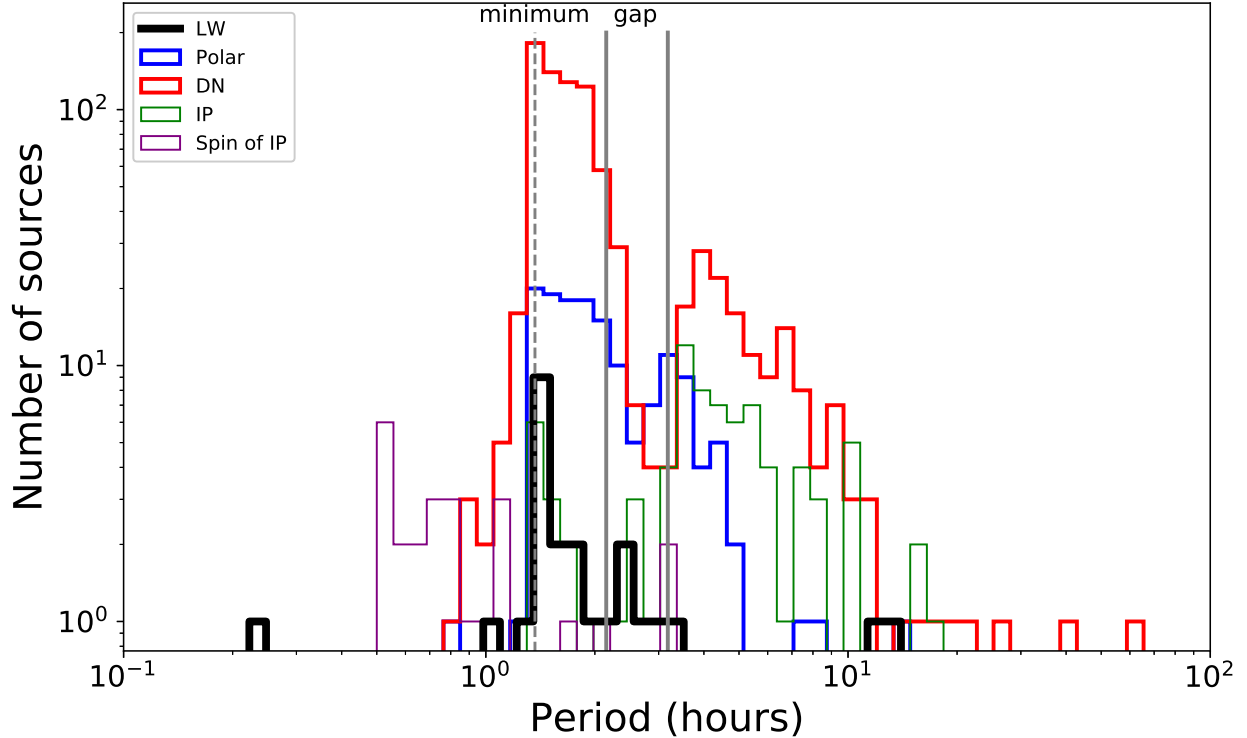


Figure 7. The period distribution of the LW sources (black histogram), in comparison with the spin (purple) and orbital (green) periods of IPs, the orbital period of polars (blue), and the orbital period of DNe from the catalog of [Ritter & Kolb \(2003\)](#), version 7.20. The period gap of CVs is delineated by a pair of vertical solid lines, and the period minimum is shown by a vertical dashed line, the values of which are taken from [Knigge et al. \(2011\)](#).

#4, #5, #9, #12, #13, #15, #16, #17, and #23. On the other hand, if $i + \beta + \epsilon < 90^\circ$, the hard X-ray-emitting pole would be always visible (the so-called “one-pole” behavior), producing a roughly constant light curve, although under certain condition ($\beta < i$) dips can be present due to obscuration by the accretion stream ([Hellier 2001](#)). The “one-pole” case generally does not favor a robust detection of the period.

IPs share the above two-pole and one-pole behavior. In addition, the orbital modulation can result in obscuration by the companion star, by the accretion stream, or by the “disc overflow” ([Norton et al. 1996](#)). Thus the light curve shape of IPs is often complex and can exhibit both sinusoidal variations and dips. Examples of this kind are found in sources #3, #7, #11, #18 and #20, although we cannot rule out the possibility of “one-pole” polars obscured by the accretion stream. We also consider source #19 a likely IP, for it has both the highest X-ray luminosity ($9.3 \times 10^{32} \text{ erg s}^{-1}$) among all sources. Notably, its sinusoidal-like variation also has the lowest amplitude ($\sim 20\%$) among all sources, which might be due to orbital modulation by a disc overflow. Source #24, which has a similar light curve as #19 and the second longest period among all sources, is also likely an IP.

The most robust identification of IPs is to detect both the spin and orbital periods. Among our sources, #1/#14 and #21/#22 show dual periods. For #1, the period is 853.8 sec and the corresponding phase-folded light curve is consistent with the two-pole behavior (Figures 4). This is naturally understood in terms of a spin modulation. In the meantime, the phase-folded light curve of #14 shows a dip at phase 0.9–0.1, which may be understood as obscuration by

the accretion stream, i.e., an orbital modulation. The corresponding orbital period of 5608.2 sec is reasonable for an IP. The two periods of #21 and #22 differ by only 5% from each other (9877.5 sec vs. 10342.3 sec). The light curve of #22 exhibits a prominent narrow dip near phase 0.5 (Figure 5). This is a clear sign of eclipse when viewed from a high inclination, thus the period of #22 should be the orbital period. On the other hand, the light curve of #21 resembles the two-pole behavior and is best understood as due to spin modulation. In this regard, source #21/#22 is probably an IP or a so-called asynchronous polar.

It is worth asking, if some of the aforementioned sources (e.g., #3, #7, #11, #18, #19, #20 and #24) were indeed IPs, why only their orbital period is detected. One plausible explanation is that their spin period, presumably below ~ 1 hour, escapes detection due to a relatively low detection efficiency. Our simulations (Section 3.3) suggest that for moderate total counts and moderate variation amplitude, the detection rate is generally low for short periods. This effect may apply in all those seven candidate IPs except #19, which has total counts of 3402. Perhaps this source has a very low spin modulation due to the “one-pole” behavior. On the other hand, source #2, which has not been discussed so far, shows a period of 3820.8 sec, significantly lower than the canonical orbital period minimum of ~ 82 minutes determined from both observations ([Gänsicke et al. 2009](#)) and theoretical modelling ([Knigge et al. 2011](#)). Thus this period is more likely the spin period. In this regard, a spike-like feature in the phase-folded light curve of #2 may be caused by a bright spot on the WD surface. The unseen orbital modulation may be due to a low inclination angle.

In DNe (i.e., non-magnetic CVs), hard X-rays are produced in the boundary layer near the WD surface, in which case spin modulation is essentially absent and orbital modulation is also expected to be weak, unless the inclination angle is sufficiently large to allow for a total eclipse. Among the 25 periodic signals, no clear sign of total eclipse is seen except for the case of #22. However, we have argued in the above that source #21/#22 is an IP because of the dual periods. Therefore, we probably have not detected any DN among the periodic sources. This is consistent with the low detection rates for eclipse predicted by our simulations in Section 3.3.

Lastly, we remark on the possible non-CV source #25. This source has an unabsorbed 1–8 keV luminosity of 8.4×10^{30} erg s⁻¹, the lowest among all 23 sources. Its X-ray spectra, characterized by a best-fit plasma temperature of 2.3 keV (notably with large uncertainties; Table 3), is also the softest among all sources. These values are more typical of ABs. Moreover, the phase-folded light curve of #25 suggests that the X-ray flux drops to the background level for nearly half of the 47317-sec period (Figure B1). As mentioned in the above, this may be due to a polar producing hard X-rays from only one pole. However, we consider such a case rather unlikely, since the corresponding period is much larger than that of any previous known polars (Figure 7), which would imply for an exceptionally strong magnetic field in the WD. Alternatively and more likely, this can be explained by a total eclipse lasting for half cycle. In this case, the eclipsed star cannot be a WD, because of the mismatch between the stellar radius (order 10^4 km) and the orbital separation (order 10^7 km). Rather, the eclipsed star is likely to have a size not much smaller than the orbital separation, suggesting an AB system viewed nearly edge-on. However, the near-zero flux for half-cycle is unusual for ABs. One possibility is that this system consists of a Sun-like star and an A-star, the latter producing no significant X-rays due to a very weak surface magnetic field (Güdel 2004). An orbital separation of $4 R_{\odot}$ estimated from the period is compatible with such a system.

In summary, based on the X-ray properties of the periodic sources, in particular their phase-folded light curves, we identify 13 candidate polars, 2 probable plus 7 candidate IPs, and one probable AB. Admittedly, polars and IPs share similar characteristics in their phase-folded light curves, as described above. The non-detection of the spin period (or orbital period in the case of #2) brings about substantial uncertainty in the IP identification. It is also noteworthy that only two long (> 3.5 hours) periods are found among the 22 orbital periods (3 probable spin periods subtracted). This fraction ($\sim 9\%$) is significantly smaller than the fraction of long-period magnetic CVs (IPs plus polars) in the solar neighborhood ($\sim 30\%$ according to the catalog of Ritter & Kolb 2003, version 7.20). This cannot be due to a selection effect of the GL algorithm, because our simulations in Section 3.3 predict that the detection rate is generally higher for longer periods. Hong et al. (2012) noticed the narrow period distribution (1–3 hours) of the 10 sources they detected and the similarity with the period distribution of polars in the solar neighborhood (Figure 7), based on which they suggested that all these 10 sources are polars. However, this could be due to an age effect, in the sense that CVs in the LW (Galactic bulge) are predominantly old and have substantially shrunk their orbitals, while CVs in the solar neighborhood can comprise of younger populations and have presently wider orbits.

6.3 CV populations in the inner Galactic bulge

In the previous section, we have classified, with a varied degree of confidence, the 23 periodic sources, finding that the vast majority

of them are either polars or IPs. Based on this classification, we now take one step forward to place constraints on the fraction of different sub-classes of CVs in the inner Galactic bulge, provided that the LW is a representative field.

The observed number of a given sub-class, for instance, polars, can be expressed as,

$$N_{\text{det,polar}} = P_{\text{det}} \times g \times \alpha_{\text{polar}} \times N_{\text{tot}}, \quad (4)$$

where N_{tot} is the total number of CVs in the LW, α_{polar} is the intrinsic fraction of polars among all CVs, g is a geometric factor that determines the detectability of a periodic signal due to spin/orbital modulations, and P_{det} is the detection probability due to the GL algorithm. Here we take $N_{\text{tot}} = 600$ ($= 667 \times 90\%$), effectively subtracting 10% of all LW sources with 1–8 keV total counts great than 100, which is the roughly the fractional contribution from the cosmic X-ray background in the LW (Zhu et al. 2018). This implicitly assumes that all 600 sources are CVs and that CVs with similar or larger total counts have been detected in 100% completeness.

We further assume that the substantial sinusoidal variation occurs only in the “two-pole” situation, that is, only one pole produces the hard X-rays and for this pole $i + \beta + \epsilon > 90^\circ$. Adopting an 50% probability to fulfill each of these two conditions, this allows us to take $g_{\text{polar}} = 50\% \times 50\% = 25\%$. In reality, P_{det} depends on the period, variation amplitude and total counts (Section 3.3). We make use of our simulation results to estimate P_{det} with the following approximations: (i) The short and long orbital periods (below or above 3.2 hours) are represented by $P=5540$ sec and $P=45540$ sec, respectively. A weight of 82% (18%) is assigned to the short (long) period, roughly according to the distribution of solar neighborhood polars; (ii) the amplitude is evenly sampled between 0.5 to 0.9, neglecting the contribution from any lower amplitudes (i.e., $P_{\text{det}} = 0$ in this case); (iii) the observed sources are grouped into different bins of total counts, from $C=75$ to 3575 cts at a step of 100 cts. Then in each bin the number of polars is predicted to be,

$$N_{\text{det,polar}}^i = g_{\text{polar}} \times \alpha_{\text{polar}} \times P_{\text{det}}^i \times N^i, \quad (5)$$

where N^i is the intrinsic number of sources in the bin, i.e., $\sum N^i = N_{\text{tot}} = 600$. $N_{\text{det,polar}}^i$ is constrained by the number of actually detected polars in a given bin. We take $\sum N_{\text{det,polar}}^i = 20$, effectively counting all the periodic sources except the two probable IPs and the one probable AB (Section 6.2). Figure 8 compares the number of detected and predicted polars as a function of total counts, which apparently agree well with each other. This then requires $\alpha_{\text{polar}} \approx 18\%$. Strictly speaking, this value is an upper limit, since a fraction of the 20 periodic sources could be IPs and g_{polar} may be significantly underestimated. For comparison, the fraction of polars is 13.5% among all known CVs in the solar neighborhood as cataloged by Ritter & Kolb (2003). This lends support to our above estimates.

A similar approach can be applied to constrain the fraction of IPs, by evaluating the detectability of spin modulation. We still adopt $g_{\text{IP}} = 25\%$ for detectable two-pole behavior. The detection rate of the GL algorithm is now represented by our simulations having a test period of $P = 554$ sec, which is suitable for the spin period. In Section 6.2, we identify three periods as probable spin period of IPs (#1, #2 and #21). Hence, according to their total counts, we estimate the fraction of IPs to be $\alpha_{\text{IP}} \approx 5\%$ in the LW. This is to be contrasted with 8.6% in the solar neighborhood (Ritter & Kolb 2003). By face value, the above estimates imply that $\sim 23\%$ of all CVs in the LW are magnetic (polars plus IPs), although we should caution that in our above approach the assumed geometry for polars and IPs are not exclusive.

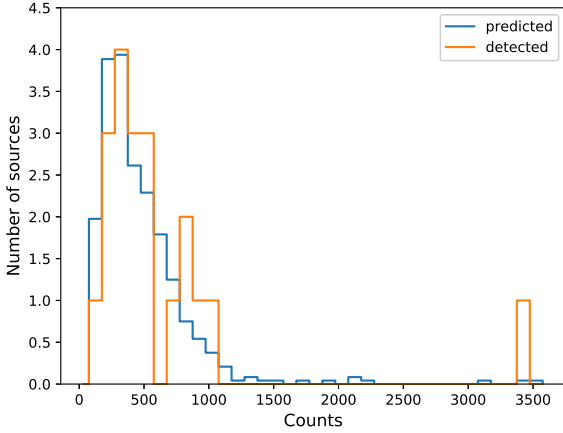


Figure 8. The comparison between the number of predicted and actually detected polars, as a function of detected counts number of sources.

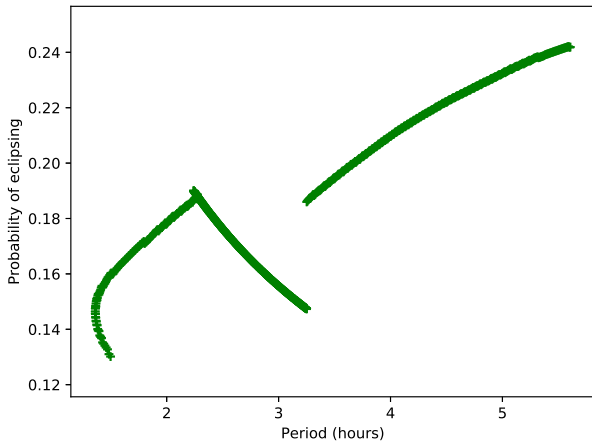


Figure 9. Probability of eclipsing in CVs. The break around 3.2 hours results from different mechanisms of angular momentum loss above and below the period gap (Knigge et al. 2011). The overall descending trend as period going down is resulted from the faster decrease of R_2 than the shrinking of separation. The climbing trend within the period gap is due to the donor star deviating from thermal equilibrium, when the binary evolves as a detached binary with period decreasing as R_2 invariant.

As discussed in Section 6.2, there is probably no DN among our periodic sources, the detection of which generally requires a total eclipse. The geometry of a WD eclipse is relatively well defined, given the inclination angle (i), the WD radius (R_{WD}), the radius of the secondary (R_2) and the orbital separation (a), together satisfying:

$$a \times \cos i \leq R_{WD} + R_2. \quad (6)$$

Physically motivated values of R_2 and a can be obtained from synthesis simulations of CVs (Knigge et al. 2011), while R_{WD} is fixed at a value corresponding to $M_{WD} = 0.75 M_\odot$. Assuming that inclination angle is evenly distributed between (0° , 90°), the probability of eclipsing, i.e., g_{DN} , is derived and plotted as a function of orbital period (related to a via Kepler’s third law) in Figure 9.

We then utilize the simulation results for eclipse (Figure 3) to

estimate the detection probability due to the GL algorithm. Specifically, we assign a weight of 83% (17%) for the representative period of 5258 (15258) sec for cases below (above) the period gap. These fractions are again taken from the statistics of solar neighborhood DNe (Figure 7). A substantial uncertainty lies in the total counts. The X-ray luminosity of DNe are typically below $10^{32} \text{ erg s}^{-1}$ (Xu et al. 2016), hence we consider only the detection rates for total counts below 575, very roughly equaling to this luminosity threshold. Requiring that the number of detectable eclipsing DNe is less than one (because we see none), we can place an upper limit of $\sim 62\%$ for α_{DN} , the intrinsic fraction of DNe in the LW.

The inconformity between this fraction to that constrained by the former two (1-18%-5%=77%) may be explained by the shorter period of CVs in the LW (see Section 6.2), since the detection rate of eclipse model highly dependent on the period. The α_{DN} could be restricted back to 77% if the fraction of short period rises to 91%. This value can still be credible based on the time scale below and beyond the period gap, simulated by the best-fit model of CV evolution in Knigge et al. (2011), i.e., 0.24 and 2.6 Gyr.

7 SUMMARY

We have searched for periodic X-ray sources in the Limiting Window, taking advantage of ~ 1 Ms *Chandra* observations and the Gregory-Loredo algorithm. Our main findings include:

- We have discovered 23 periodic sources with 25 signal in the LW by using GL method, including 10 of them already found by LS method in Hong et al. (2012). Their luminosity over 1-8 keV range locates at $10^{31} - 10^{33} \text{ erg s}^{-1}$. The general feature of these 23 sources resembles that of mCVs, including both polars and IPs.
- We provide estimation on fraction of polars and IPs in the total CV sample, i.e., 18% and 5% respectively. While the relatively low estimation on DNe (62%) indicates the shorter period distribution of CV in the LW.
- The lower luminosity and narrow eclipsing model for orbital modulation reduced the detection rate simultaneously for periodicity. That may explain why we had no trace on non-mCVs in GCR in earlier period searching work.
- We proved the higher detection rate, more usage of data and ignorance of observation gap for GL method compared with LS method. It is noteworthy that the shape of light curve in GL method could be modified according to different scenarios. It was applied on detection of planetary transits by using customized eclipsing model (Aigrain & Favata 2002). For the utility of GL method, there is still room for improvement in the future.

We thank Xiaojie Xu and Zhenlin Zhu for helpful discussions. This work is supported by the National Key Research and Development Program of China under grant 2017YFA0402703.

REFERENCES

- Aigrain S., Favata F., 2002, *A&A*, **395**, 625
 Buccheri R., et al., 1983, *A&A*, **128**, 245
 Cheng Z., Li Z., Li X., Xu X., Fang T., 2019, *ApJ*, **876**, 59
 Cicuttin A., Colavita A. A., Cerdeira A., Mutihac R., Turrini S., 1998, *ApJ*, **498**, 666
 Deeming T. J., 1975, *Ap&SS*, **36**, 137
 Edelson R. A., Krolik J. H., 1988, *ApJ*, **333**, 646
 Gänsicke B. T., et al., 2009, *MNRAS*, **397**, 2170
 Gregory P. C., Loredo T. J., 1992, *ApJ*, **398**, 146

- Güdel M., 2004, *A&ARv*, **12**, 71
 Hailey C. J., et al., 2016, *ApJ*, **826**, 160
 Heise J., Brinkman A. C., Gronenschild E., Watson M., King A. R., Stella L., Kieboom K., 1985, *A&A*, **148**, L14
 Hellier C., 2001, *Cataclysmic Variable Stars*
 Hong J., 2012, *MNRAS*, **427**, 1633
 Hong J. S., van den Berg M., Grindlay J. E., Laycock S., 2009, *ApJ*, **706**, 223
 Hong J., van den Berg M., Grindlay J. E., Servillat M., Zhao P., 2012, *ApJ*, **746**, 165
 Knigge C., Baraffe I., Patterson J., 2011, *ApJS*, **194**, 28
 Leahy D. A., Darbro W., Elsner R. F., Weisskopf M. C., Sutherland P. G., Kahn S., Grindlay J. E., 1983, *ApJ*, **266**, 160
 Lomb N. R., 1976, *Ap&SS*, **39**, 447
 Morihana K., Tsujimoto M., Yoshida T., Ebisawa K., 2013, *ApJ*, **766**, 14
 Munro M. P., Baganoff F. K., Bautz M. W., Brandt W. N., Garmire G. P., Ricker G. R., 2003, *ApJ*, **599**, 465
 Munro M. P., et al., 2009, *ApJS*, **181**, 110
 Norton A. J., Beardmore A. P., Taylor P., 1996, *MNRAS*, **280**, 937
 Revnivtsev M., Sazonov S., Churazov E., Forman W., Vikhlinin A., Sunyaev R., 2009, *Nature*, **458**, 1142
 Revnivtsev M., Sazonov S., Forman W., Churazov E., Sunyaev R., 2011, *MNRAS*, **414**, 495
 Ritter H., Kolb U., 2003, *A&A*, **404**, 301
 Sazonov S., Revnivtsev M., Gilfanov M., Churazov E., Sunyaev R., 2006, *A&A*, **450**, 117
 Scargle J. D., 1982, *ApJ*, **263**, 835
 Schuster A., 1898, *Terrestrial Magnetism (Journal of Geophysical Research)*, **3**, 13
 Schwarzenberg-Czerny A., 1996, *ApJ*, **460**, L107
 Silber A. D., 1992, PhD thesis, MASSACHUSETTS INSTITUTE OF TECHNOLOGY.
 Stellingwerf R. F., 1978, *ApJ*, **224**, 953
 Wevers T., et al., 2016, *MNRAS*, **462**, L106
 Xu X.-J., Wang Q. D., Li X.-D., 2016, *ApJ*, **818**, 136
 Xu X.-J., Li Z., Zhu Z., Cheng Z., Li X.-d., Yu Z.-l., 2019, *ApJ*, **882**, 164
 Zhu Z., Li Z., Morris M. R., 2018, *ApJS*, **235**, 26
 van den Berg M., Hong J. S., Grindlay J. E., 2009, *ApJ*, **700**, 1702

APPENDIX A: A BRIEF INTRODUCTION TO THE GREGORY-LOREDO ALGORITHM

The basic rules for Bayesian probabilities are the sum rule,

$$p(H_i|I) + p(\bar{H}_i|I) = 1, \quad (\text{A1})$$

and the product rule,

$$p(H_i, D|I) = p(H_i|I) \cdot p(D|H_i, I) = p(D|I) \cdot p(H_i|D, I). \quad (\text{A2})$$

From Eqn. A2 we can derive Bayes's theorem,

$$p(H_i|D, I) = p(H_i|I) \cdot \frac{p(D|H_i, I)}{p(D|I)}. \quad (\text{A3})$$

The symbols here follow Gregory & Loredó (1992). Specifically, p is the Bayesian posterior probability, H_i denotes the i -th hypothesis, D for the data, and I for the ensemble of all hypotheses, i.e., all the model used. The GL algorithm employs a stepwise function to detect periodic signal. Each model has $(m+2)$ parameters: the angular frequency $\omega = 2\pi/P$ (P is the period), the phase parameter ϕ , and m values of r_j , which denotes the count rate in each phase bin where $j=1$ to m . In the following we replace H_i by M_i to denote the model where i represents the number of bins in the stepwise model. Then the Bayes's theorem can be written as,

$$p(M_i|D, I) = p(M_i|I) \cdot \frac{p(D|M_i, I)}{p(D|I)}. \quad (\text{A4})$$

We can write $I = M_1 + M_2 + M_3 + \dots$, where “+” stands for “or”. Thus the proposition (M_i, I) is true if and only if model M_i is true, i.e. $(M_i, I) = M_i$. The GL algorithm defines an odds ratio for model comparison,

$$O_{ij} = \frac{p(M_i|D, I)}{p(M_j|D, I)} = \frac{p(M_i|I)}{p(M_j|I)} \cdot \frac{p(D|M_i)}{p(D|M_j)} \quad (\text{A5})$$

Note that M_1 means a constant model, M_i ($i=2,3,4,\dots,N_{\text{mod}}$, where N_{mod} is the total number of models considered) represents a periodic model. The probability for each model can be deduced from Eqn. A5,

$$p(M_i|D, I) = O_{i1} \cdot p(M_1|D, I), \quad (\text{A6})$$

thus

$$p(M_1|D, I) = \frac{\sum_{j=1}^{N_{\text{mod}}} p(M_j|D, I)}{\sum_{j=1}^{N_{\text{mod}}} O_{j1}} = \frac{1}{\sum_{j=1}^{N_{\text{mod}}} O_{j1}}. \quad (\text{A7})$$

Substituting Eqn. A7 into Eqn. A6, we have

$$p(M_i|D, I) = \frac{O_{i1}}{\sum_{j=1}^{N_{\text{mod}}} O_{j1}}. \quad (\text{A8})$$

Then the probability of a periodic signal is

$$p(M_m(m > 1)|D, I) = \frac{\sum_{m=2}^{m_{\text{max}}} O_{m1}}{1 + \sum_{m=2}^{m_{\text{max}}} O_{m1}}, \quad (\text{A9})$$

where m_{max} is the maximum value of m . The odds ratio can be calculated from the probability of the model,

$$O_{m1} = \frac{p(M_m|D, I)}{p(M_1|D, I)}. \quad (\text{A10})$$

Using Bayes's theorem (Eqn. A4),

$$O_{m1} = \frac{p(M_m|I) \cdot p(D|M_m)}{p(M_1|I) \cdot p(D|M_1)}. \quad (\text{A11})$$

Following the assignment by Gregory & Loredó (1992), we assume that the periodic and aperiodic signals have the same probability. Then the priors for the models can be written explicitly as,

$$p(M_1|I) = \frac{1}{2}, \quad (\text{A12})$$

$$p(M_m|I) = \frac{1}{2^v}, \quad v = m_{\text{max}} - 1. \quad (\text{A13})$$

For astronomical data of Poisson distribution, it can be shown that (Equation 5.27 in Gregory & Loredó 1992),

$$p(D|M_m) = \frac{\Delta t^N (m-1)! N! \gamma(N+1, A_{\text{max}}) T}{2\pi A_{\text{max}} (N+m-1)! T^{N+1} \ln(\omega_{\text{hi}}/\omega_{\text{lo}})} \times \int_{\omega_{\text{lo}}}^{\omega_{\text{hi}}} \frac{d\omega}{\omega} \times \int_0^{2\pi} d\phi \frac{m^N}{W_m(\omega, \phi)}, \quad (\text{A14})$$

where ω_{lo} and ω_{hi} are the lower and upper bounds of the frequency range. It should be emphasized that the above equation holds for the case in which the period and phase are both unknown. Substituting $m=1$ into Eqn. A14, we have

$$p(D|M_1) = \frac{\Delta t^N N! \gamma(N+1, A_{\text{max}}) T}{A_{\text{max}} N! T^{N+1}}. \quad (\text{A15})$$

Substituting Eqns. A12, A13, A14 and A15 into Eqn. A11, the odds ratio can be written as follows, which is the same as Equation 5.28

in Gregory & Loredo (1992),

$$O_{m1} = \frac{1}{2\pi\nu \ln(\omega_{\text{hi}}/\omega_{\text{lo}})} \binom{N+m-1}{N}^{-1} \times \int_{\omega_{\text{lo}}}^{\omega_{\text{hi}}} \frac{d\omega}{\omega} \times \int_0^{2\pi} d\phi \frac{m^N}{W_m(\omega, \phi)} \quad (\text{A16})$$

Astronomical data are often subject to observational gaps. This may result in unevenly covered phase bins, leading to spurious detections especially at low frequencies. Gregory & Loredo (1992) provides a solution to this problem, by introducing a weighting factor

$$S(\omega, \phi) = \prod_{j=1}^m s_j^{-n_j}, \quad (\text{A17})$$

$$s_j(\omega, \phi) = \frac{\tau_j(\omega, \phi)}{T/m}, \quad (\text{A18})$$

where T is the total time span between the first and last photons and $\tau_j(\omega, \phi)$ denotes the exposure time in each phase bin. Then the odds ratio should be modified as,

$$O_{m1} = \frac{1}{2\pi\nu \ln(\omega_{\text{hi}}/\omega_{\text{lo}})} \binom{N+m-1}{N}^{-1} \times \int_{\omega_{\text{lo}}}^{\omega_{\text{hi}}} \frac{d\omega}{\omega} \times \int_0^{2\pi} d\phi \frac{S(\omega, \phi)m^N}{W_m(\omega, \phi)}. \quad (\text{A19})$$

Ultimately, the probability of whether the dataset is periodic is,

$$p(\text{periodic}) = \frac{\sum_{m=2}^{m_{\text{max}}} O_{m1}}{1 + \sum_{m=2}^{m_{\text{max}}} O_{m1}}. \quad (\text{A20})$$

The posterior probability of the frequency contains the period of the signal,

$$O_{m1}(\omega) = \frac{1}{2\pi\nu} \binom{N+m-1}{N}^{-1} \times \int_0^{2\pi} d\phi \frac{S(\omega, \phi)m^N}{W_m(\omega, \phi)}. \quad (\text{A21})$$

The period locates at $P = 2\pi/\omega$ when $O_{m1}(\omega)$ takes the highest value.

APPENDIX B: ADDITIONAL FIGURES OF THE PERIODIC X-RAY SOURCES



Figure B1. Each row shows one periodic source. *Left:* The 1–8 keV phase-folded light curve at the modulation period. The green dashed line represents the mean count rate, whereas the yellow strip represents the local background, the width of which represents 1σ Poisson error. *Middle:* the 1–8 keV long-term, inter-observation light curve. Arrows represent 3σ upper limits. *Right:* Source spectrum and the best-fit model.



Figure B2. Continued

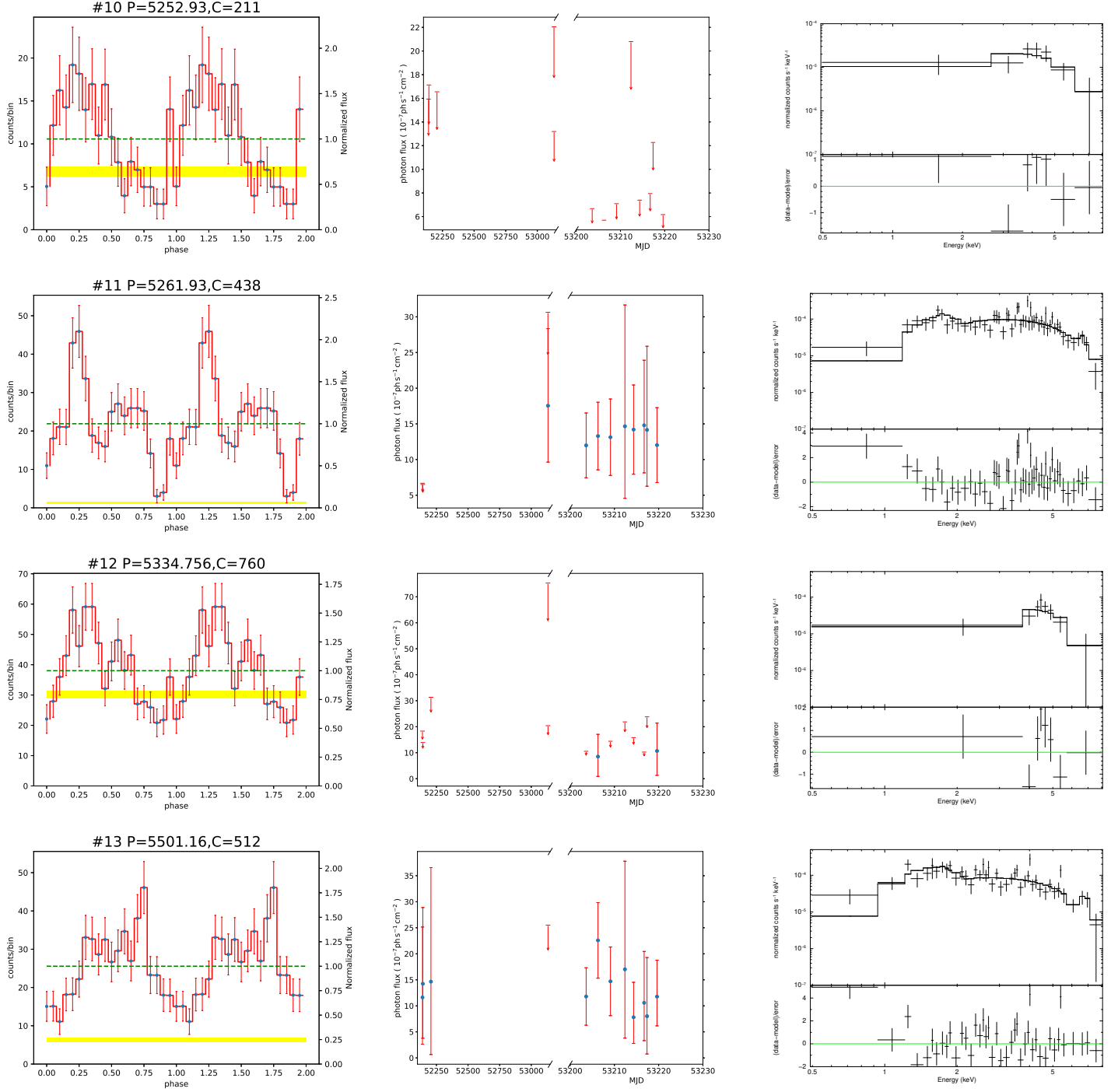


Figure B3. Continued

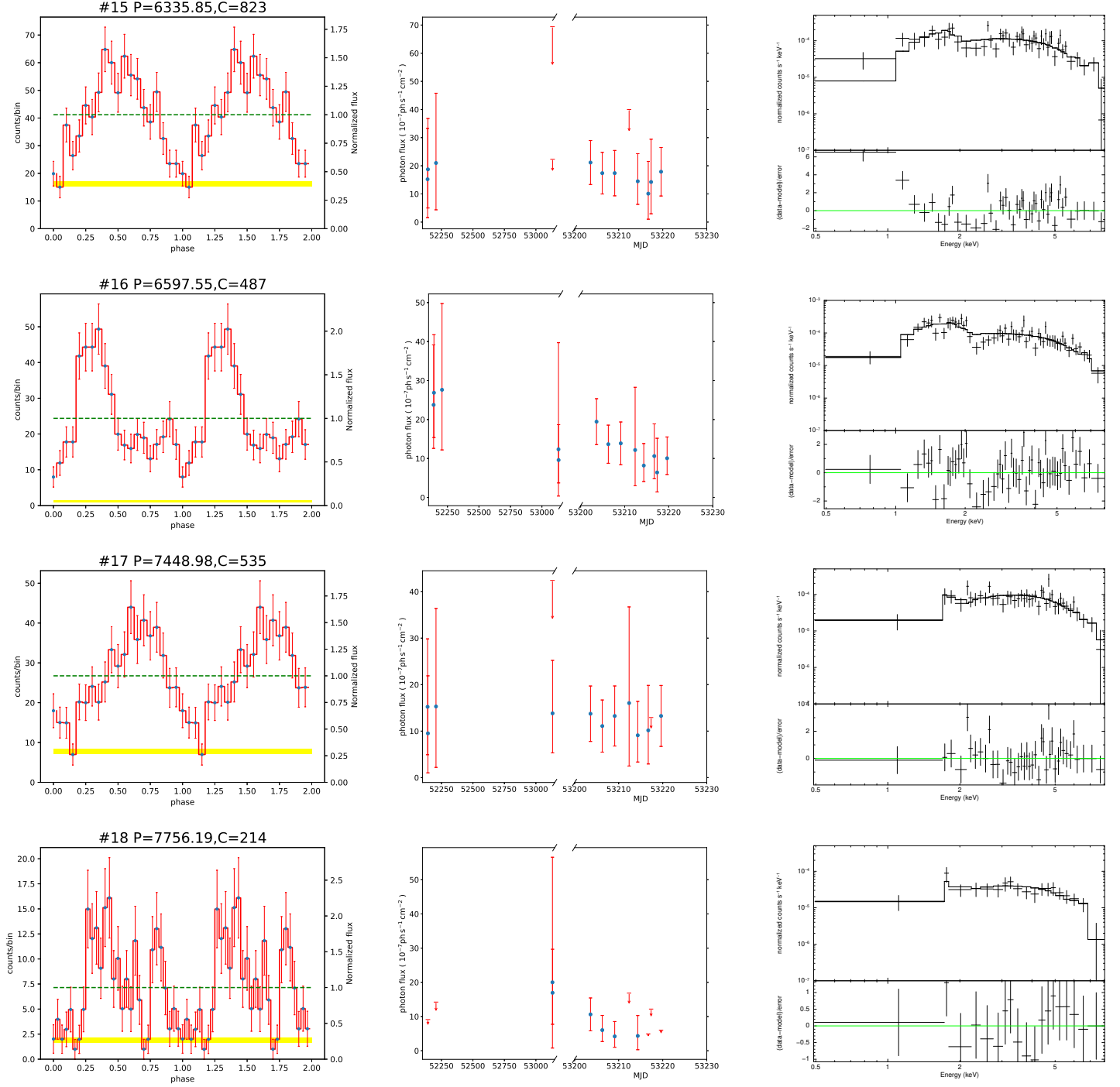


Figure B4. Continued



Figure B5. Continued



Figure B6. Continued